Lab on a Chip

PAPER

View Article Online
View Journal | View Issue

Cite this: *Lab Chip*, 2026, **26**, 2834

Band-stop microfluidics for high-purity, label-free enrichment of viable cancer cells from whole blood

Lewis Krzeczkowski,[a] Georgios Nteliopoulos,[a] Simak Ali,[a] Paul Davey,[b] R. Charles Coombes[a] and Ali Salehi-Reyhani *[ac]

Liquid biopsy requires the isolation of viable circulating tumour cells (CTCs) from whole blood at high purity and with sufficient quality for functional assays. These requirements are not readily met by either label-based methods or size-only low-pass filters. Antibody labels can be specific yet miss phenotypically diverse CTCs, while size-based approaches may capture more broadly but suffer from leukocyte contamination. Here, we introduce a microfluidic band-stop filter that implements a size-selective transfer function, replacing a single threshold with an engineered peaked size-capture response. This is achieved by coupling hydrodynamic filtering with hydrodynamic trapping in a high-density array. Small cells follow streamlines that pass through trap apertures, intermediate-sized cells are admitted but retained by downstream constrictions, whereas larger cells occupy streamlines displaced from the channel wall and are hydrodynamically transported past the traps. As a result, only cells with diameters within the band-stop window are retained, while both smaller and larger cells pass. Using rigid microspheres, the device exhibits a canonical band-stop profile. Using cultured cell lines, capture efficiency peaks for CTC-like diameters and is suppressed for leukocyte-sized cells. Critically, the behaviour is preserved in undiluted, full haematocrit whole blood, where no leukocyte retention is observed and target-sized cancer cells are selectively enriched without fouling at capture efficiencies comparable to commercial systems. Trapped cells tolerate buffer exchange and on-chip drug exposure, where responses were concordant with matched off-chip culture. Cells are released on demand and expanded off-chip, confirming post-processing viability.

Received 13th January 2026,
Accepted 26th March 2026

DOI: 10.1039/d6lc00039h

rsc.li/loc

Introduction

Circulating tumour cells (CTCs) are exceedingly rare in peripheral blood, often present at only 1–10 CTCs per mL of blood amidst billions of haematologic cells.[1] In practical terms, this translates to roughly one tumour cell per 10^6–10^7 leukocytes and $>10^9$ erythrocytes. The isolation of such scarce CTCs from whole blood is a formidable "needle-in-a-haystack" problem. Compounding the challenge, CTCs are highly heterogeneous and can resemble blood cells in size or deformability, which makes purely physical separations difficult. For example, some CTCs overlap in size with larger white blood cells (WBCs), meaning a size-based filter may inadvertently retain WBCs or even clog with them.[2,3] On the other hand, CTCs that have undergone phenotypic changes may lose traditional tumour markers, complicating biochemical or antibody-based isolation. An effective enrichment method must therefore sift out a handful of CTCs from the background of blood cells while accounting for CTC variability in size, deformability, and antigen expression – all without compromising cell integrity. This challenge has driven the development of both labelled and label-free CTC isolation strategies.[4,5]

The dominant clinical CTC isolation methods use affinity or label-based capture, typically targeting epithelial markers. The FDA-approved CellSearch system, for instance, employs anti-EpCAM antibodies to capture CTCs from blood. Such positive-selection platforms have demonstrated clinical utility, but they suffer well-documented drawbacks.[6–8] CTCs that have undergone epithelial–mesenchymal transition (EMT) can downregulate EpCAM and other epithelial antigens, causing these cells to evade detection by antibody-based methods.[9–12] Indeed, CellSearch recovers as little as ~2% of CTCs from certain mesenchymal cancer cell lines.[8] Moreover, label-based systems often co-enrich non-target WBCs, yielding low-purity samples with significant numbers of contaminating leukocytes (often <0.1% CTC purity). Such contamination not only complicates analysis (*e.g.* confounding molecular assays with

[a] *Department of Surgery & Cancer, Imperial College London, London, W12 0HS, UK. E-mail: ali.salehi-reyhani@imperial.ac.uk*
[b] *Oncology Medicinal Chemistry, R&D AstraZeneca, The Discovery Centre, Biomedical Campus, 1 Francis Crick Avenue, Cambridge, CB2 0AA, UK*
[c] *Institute for Molecular Science and Engineering, Imperial College London, SW7 2AZ, UK*

WBC background) but also precludes insights into CTC viability, since many clinical workflows fix and stain captured cells. While refinements like negative depletion (removing WBCs by targeting CD45) or combined marker panels can improve purity, the fundamental limitation remains.[13] Any method relying on specific biomarkers risks missing the very CTC subpopulations (EMT-transformed, stem-like, or atypical phenotypes) that are most clinically aggressive.

In contrast, label-free methods aim to enrich CTCs based on inherent physical properties – most commonly size, deformability, or density – without the need for tumour-specific antibodies.[14–17] Microfluidic technologies have been at the forefront of this label-free paradigm.[18] CTCs are generally larger and less deformable than blood cells, which has inspired size-exclusion filters and inertial focusing devices to separate CTCs from smaller red cells and most leukocytes.[19,20] For a comprehensive overview, the reader is directed toward several reviews covering microfluidic-based separation of CTCs.[4,21–23] The advantage of label-free techniques is their unbiased capture of CTCs regardless of surface markers – for example, EpCAM-negative or mesenchymal CTCs and even CTC clusters can be retained based on size alone. Label-free enrichment also tends to preserve cell viability by avoiding harsh chemical labelling or fixation steps. However, purely physical methods face their own trade-offs. Size- or deformability-based filters must contend with the wide size distribution of CTCs and overlap with WBC populations. Rigid or larger-than-average WBCs (such as neutrophils or monocytes) can be unintentionally captured, diminishing purity, while very small or highly deformable CTCs might escape capture entirely. Filtration devices may clog due to dense blood cell loads, requiring pre-dilution or frequent filter replacement. Thus, although label-free systems broaden the spectrum of CTCs that can be enriched and maintain cell integrity, they often struggle to simultaneously achieve high recovery and high purity.

Several commercial platforms have embraced label-free CTC enrichment, with the Parsortix system being a prominent example.[24] Parsortix employs a microfluidic cassette that gradually narrows to a critical gap (approximately 6.5 μm) through which blood is flowed. Smaller and more deformable cells (erythrocytes and most WBCs) squeeze through the gap, whereas larger or stiffer cells, including CTCs, are physically trapped on the upstream side. Captured CTCs have been reported to remain viable and can be released from the cassette for downstream culture or molecular analysis.[25] Parsortix and similar microfiltration devices have the ability to enrich a broad spectrum of CTC types (including EpCAM-low cells and clusters) from patient samples. Despite these advantages, the Parsortix platform exemplifies a key drawback of current label-free methods, *i.e.* significant WBC contamination in the output product. In practice, a Parsortix-enriched sample still contains on the order of 10^3–10^4 residual WBCs from each blood draw. For instance, Poggiana *et al.* documented an average of 3.3×10^3 WBC carryover (range $0.9–6.8 \times 10^3$) in Parsortix harvests per 2.5–5 mL blood processed, even though this was substantially lower than the 1.7×10^4 WBC background from CellSearch (range $0.3–3.5 \times 10^4$) on the same samples.[25] Another study comparing technologies found that Parsortix isolates had a CTC purity of only 3.1% ± 2.7%, meaning roughly 97% of cells in the final product were contaminating leukocytes, albeit this purity was marginally higher than that of the immunomagnetic platforms tested in parallel.[24] Such levels of WBC contamination can severely complicate analytical characterization of captured CTCs. First, the presence of thousands of WBCs imposes additional steps (such as immunostaining or genomic background subtraction) to distinguish true CTC signals from blood cell noise. Second, rare important subpopulations like CTC clusters or mesenchymal CTCs could be obscured or lost among the residual WBCs. Finally, any contaminant WBCs may themselves undergo activation or provide confounding mRNA/DNA background in sequencing-based analyses.[7] In summary, while platforms like Parsortix highlight the promise of label-free, viable CTC capture, they also underscore the unmet need for improved purity. An ideal system would retain CTCs with high efficiency while simultaneously depleting normal blood cells to near-zero levels, something not fully achieved by current single-step label-free devices.

To address the extreme rarity of CTCs, researchers have also focused on scaling up label-free isolation to process larger blood volumes at high flow rates. Notably, the CTC-iChip is a high-throughput microfluidic sorter that combines multiple physical principles in sequence (size-based inertial focusing and immunomagnetic negative selection) to isolate CTCs from whole blood.[26] The CTC-iChip operates in an antigen-independent manner; it can sort on the order of 10^7 cells s^{-1}, enabling the rapid handling of standard blood draws (7.5–10 mL) and efficiently recovering CTCs from both epithelial and non-epithelial cancers. By focusing the blood cells into streamlined flow lanes, then using magnetophoresis to pull out WBCs that have been weakly labelled with common leukocyte antibodies, the iChip achieves continuous, high-throughput depletion of background cells while herding unlabelled CTCs into a separate output channel. Reported performance of the initial CTC-iChip included a 99.5% median recovery of spiked cancer cells across 11 lines and residual WBC levels depending on enrichment strategy: positive selection (EpCAM+ cell-enriched) resulted in 1.5×10^3 WBCs per mL of whole blood (range $67–2.5 \times 10^3$ WBCs per mL), whereas negative selection (leukocyte depletion) resulted in 3.2×10^4 WBCs per mL (range $1.7–3.9 \times 10^4$ WBCs per mL). This exemplifies how multi-stage, hybrid designs can improve the trade-offs between yield and purity by leveraging both physical and immunological separation principles. Pushing throughput further, an ultra-high-volume workflow was recently demonstrated by integrating an inertial separation module with an optimized magnetic sorter to process diagnostic leukapheresis product samples, termed the LP (leukapheresis product) CTC-iChip.[27,28] Leukapheresis is a clinical procedure in which large volumes of blood are processed with centrifugal enrichment of peripheral blood mononuclear cells into a product of 50–100 mL; CTCs with a similar density to mononuclear cells become enriched in the LP.[29] Mishra *et al.*

showed that the ^{LP}CTC-iChip could enrich spiked CTCs from healthy donor leukopaks with 86.1 ± 0.6% recovery[27] while removing 99.97% of WBCs – an impressive feat given the initial cell load. When applied to patient samples, extremely high yields of CTCs were reported (mean 1.0×10^4 CTCs per patient; range 100 to 5.8×10^4).[28] However, even with this two-stage approach, the sheer scale of input means that a small fraction of unsorted WBCs translates to significant absolute numbers on the order of 10^4 WBCs per mL; the final purity of CTCs in the output was 0.3% on average. Thus, high-throughput, large-volume solutions, while unprecedented in the absolute number of CTCs recovered, highlight a recurring theme. CTC isolation can be scaled up, but achieving ultra-high purity concurrently remains challenging. These sophisticated platforms also tend to be complex, requiring multiple integrated steps and external fields, which could hinder widespread adoption. The state of the art, therefore, still calls for innovative strategies to realise precise, high-purity CTC enrichment in a simpler, analytically robust manner.

Given the limitations outlined above, there is a clear unmet need for a CTC isolation technology that can combine the strengths of label-free enrichment (no dependency on tumour biomarkers and preservation of cell viability) with greatly enhanced selectivity for CTCs over WBCs. In this work, we introduce a microfluidic band-stop filter for viable CTC enrichment as a new label-free approach to meet this need. In electronics, a "band-stop" filter rejects a particular band of frequencies while allowing frequencies above and below that band to pass. By analogy, our microfluidic band-stop filter is engineered to reject a particular band of cell sizes (and/or deformabilities) – specifically, the size range corresponding to

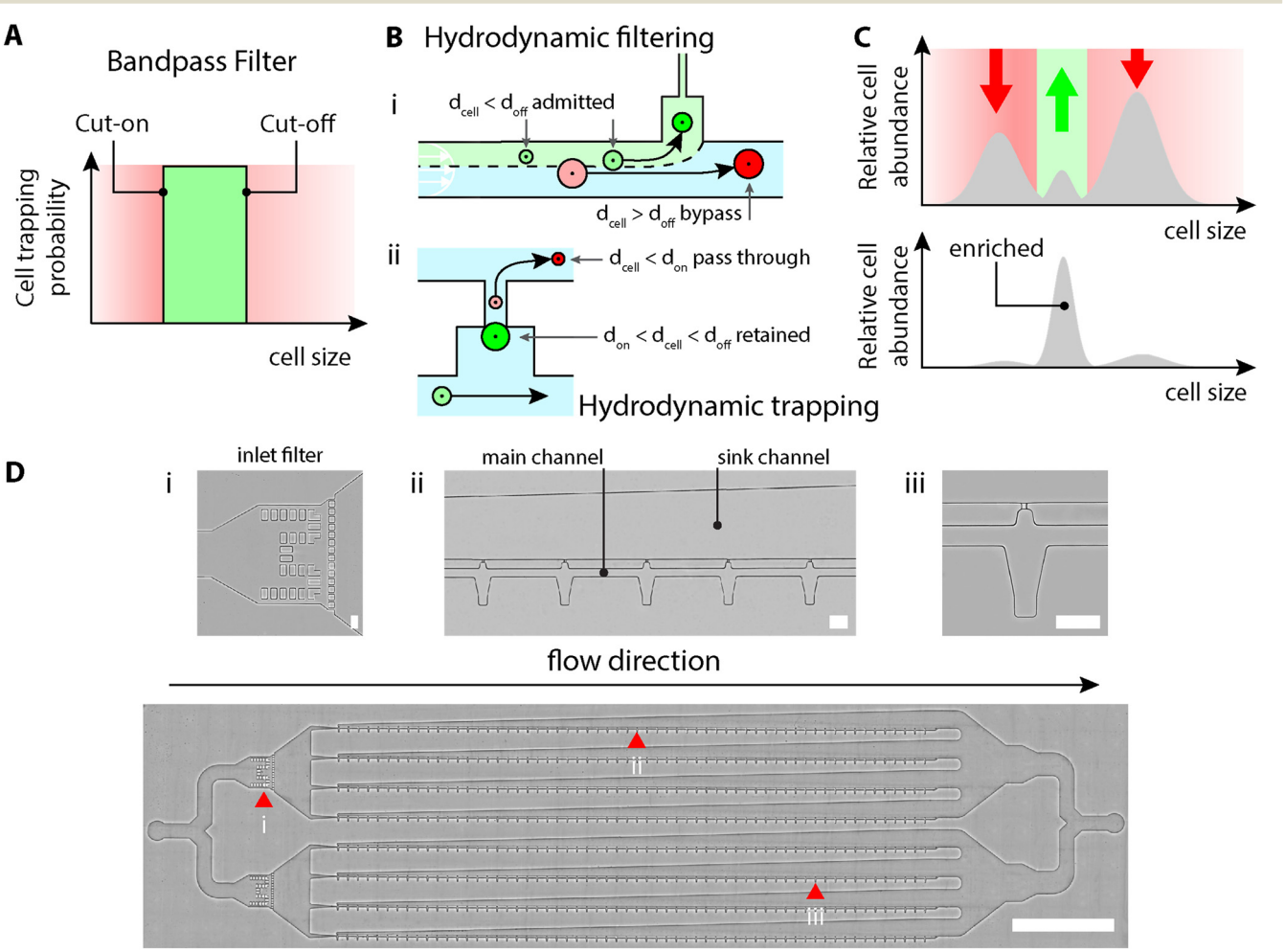

Fig. 1 Concept and implementation of a microfluidic band-stop filter. (A) Schematic transfer function of an idealised band-stop filter, where the probability of trapping is a function of cell diameter. The filter exhibits a stop-band bounded by cut-on and cut-off diameters. Only cells within a specific size range are trapped, whereas smaller and larger cells pass. (B) (i) Hydrodynamic filtering permits only cells below a threshold size to enter the filter and contributes to setting the upper cut-off feature of the filter. (ii) Hydrodynamic trapping retains only cells above a threshold size and establishes the lower bound cut-on feature of the filter. By combining these two size-selective elements a band-stop filter can be achieved. (C) Passing a mixed population of cells through the device depletes cells outside the band-stop region (red arrows) and enriches the relative abundance of cells whose size falls within (green arrow). (D) Bright-field images of the microfluidic band-stop device used for enrichment. Bottom: full device (flow direction indicated) where red arrowheads indicate the locations of the inset images. Scale bar, 5 mm. Top insets: (i) inlet debris/aggregate filter, (ii) a representative segment of the band-stop trap array, and (iii) a single trap. Scale bars for insets, 100 μm.

most WBCs – thereby permitting both smaller and larger cells to pass through. In practice, this means normal blood cells are selectively removed or diverted, whereas CTCs are retained or enriched. By removing the interfering leukocyte "band," the band-stop filter aims to output a highly purified and concentrated suspension of intact CTCs.

In the band-stop architecture (Fig. 1), size-dependent transport arises from the coupling of hydrodynamic trapping and filtering. Cells smaller than the trap aperture follow streamlines that enter the trapping sites and pass through unimpeded. Cells within an intermediate size range are admitted into the traps but cannot transit the hydrodynamic constriction, leading to stable retention under flow. Larger cells, by contrast, occupy streamlines whose centroids are displaced away from the channel wall and therefore bypass the trapping sites entirely, continuing along the main channel. The lower and upper bounds of the capture window are thus defined by hydrodynamic admission and exclusion, respectively, rather than by surface interactions or clogging.

The band-stop filter's physical cutoff parameters (*e.g.* critical gap dimensions, flow-induced forces) can be controlled and modelled, allowing the filtration performance to be tuned for different target size ranges. This enables rigorous characterisation of the device's "transfer function" in terms of cell size/deformability – analogous to measuring the frequency response of an electrical filter. Consequently, the selectivity of the band-stop filter (*i.e.* which sizes are halted *vs.* transmitted) can be systematically optimized to maximize CTC yield and purity. The approach preserves cell viability by operating under gentle hydrodynamic conditions, ensuring enriched CTCs remain suitable for downstream analyses such as culture expansion, single-cell sequencing, or functional assays. In summary, our proposed band-stop microfilter directly addresses the major pain points of existing technologies by providing label-free, size-selective, and high-purity enrichment of CTCs. Here, we detail the design, operation, and performance of this novel microfluidic filter, demonstrating how it achieves selective capture of viable CTCs from whole blood – a significant step toward more effective "liquid biopsy" workflows for cancer diagnostics and research.[30,31]

Results and discussion

Device architecture and operating principle

The trapping architecture builds on early demonstrations of cell arraying by differential fluidic resistance, most notably the work of Tan and Takeuchi, which established resistance-based trapping as a robust mechanism for positioning single cells in microfluidic arrays.[32] Additionally, the present design also builds on early demonstrations of hydrodynamic filtration, particularly the work of Yamada and Seki, which established size-dependent streamline partitioning as a basis for passive microfluidic separation.[33] Two edges of the band-stop are set by distinct hydrodynamic mechanisms (Fig. 1A). The cut-on (lower edge, d_{on}) is set by hydrodynamic trapping (Fig. 1B). The trap throat width and channel height define the minimum size that can be immobilised under flow. Objects smaller than the hydrodynamic trap width cannot occlude the entrance and are swept through; objects larger than d_{on} lodge and are retained in the cell park. Since captured cells conform elastically to the throat, a single cell fully seals the trap inlet, preventing multi-occupancy and clog cascades. The cut-off (upper edge, d_{off}) is set by hydrodynamic filtering (Fig. 1B). Before a particle can reach the trap, it must be admitted into the side-branch entrance. Only streamlines within an acceptance region adjacent to the channel wall feed the branch; particles whose centroid lies outside this region cannot kinematically enter, even if they are smaller than the branch width. The relative hydraulic resistances of the trap lane, downstream main channel and sink channel determine the partitioning of flow at each junction, which sets the acceptance-region width and, consequently, the maximum admissible diameter. This series coupling yields a finite stop-band: particles smaller than d_{on} pass because they cannot seal the trap and particles larger than d_{off} pass because they are hydrodynamically excluded from the branch. Only particles within $d_{on} \leq d \leq d_{off}$ are admitted and then immobilised in each trap; note that capture is entirely passive and hydrodynamic. For samples laden with particles having a range of sizes, this will preferentially isolate those that meet this criterion and suppress the trapping of other factors, leading to an enrichment (Fig. 1C).

We realised the band-stop behaviour in a single, passive microfluidic device that combines hydrodynamic filtering with hydrodynamic trapping in series (Fig. 1D). The chip comprises 8 parallel main channels (50 μm width × 30.25 mm length × 30 μm height), each populated with 60 identical trapping units at 500 μm pitch (total 480 traps). For metastatic breast cancer, CTCs are typically present at ~1–10 mL^{-1} in peripheral blood, corresponding to tens to hundreds of cells in a standard 7.5 mL clinical sample, although higher burdens can occur in advanced disease. The 480-trap array provides sufficient capacity to recover clinically relevant numbers of cells. The cell traps consisted of a cell park isosceles trapezoidal area (40 to 30 μm width × 30 μm length × 30 μm height) and a narrow hydrodynamic trap channel (10.0 ± 1.0 μm width × 20 μm length × 10 μm height). A trapezoidal sink channel (30 μm height) runs parallel to each main channel to receive bypass and flow through unoccupied traps; its width increases from 100 μm at the first trap to 900 μm after the final trap, maintaining a controlled pressure drop along the array. At the inlet, on-chip debris filters (50 μm sieve followed by a 26 μm barrier) protect the array from aggregates that would otherwise clog the main channels. The device operates in the Stokes regime (typical infusion 5–25 μL min^{-1} across 8 channels; Re $\ll$1). Under these gentle conditions, captured cells remain viable for extended on-chip manipulations (buffer exchange, staining, drug perfusion).

Band-stop capture profile with beads and cells

In buffer tests with beads (Fig. 2), capture efficiency peaked at 101 ± 8.3% for 12 μm microspheres, compared to only 21.1 ± 4.5% for 10 μm and 0% for 5 μm, confirming a sharp lower bound or cut-on of around 10 μm. Above the optimum, 15 μm beads were trapped at a lower 30.6 ± 6.6% efficiency and 20 μm beads at 7.8 ± 1.1%, defining an upper cut-off in this range. Without microspheres of intermediate sizes, it is difficult to measure the cut-on and cut-off regions to higher precision. We therefore estimate the full width of the stop-band as roughly 11–14 μm at 50% of peak efficiency (−3 dB point). The incomplete blockade of traps by large, rigid beads explains the gentle tail at larger diameters. For instance, 20 μm beads lodge without fully sealing the trap, so some flow, albeit at a reduced rate, continues through that trap and can draw in additional beads behind it, increasing the capture count for larger microspheres.

Next, we tested the response to cancer cell lines. Determining the bandpass response profile with cells is challenging owing to the intrinsic distribution of cell size for any given cell line and significant overlap with other lines. A screen of cell lines available in our labs was conducted for their distribution of single-cell diameter within the cell population. Cells were measured by bright-field and fluorescence microscopy detached from plates and rounded in suspension.

We chose 4 lines for their single-cell diameters that spanned the band-stop filter. The mass of their distributions falls below, within and above the band-stop, as measured using rigid microspheres (Fig. 3A). Culture medium containing cells is infused into the device and cells fitting the trapping criterion ($d_{on} \leq d \leq d_{off}$) become arrayed in traps and retained on-chip (Fig. 3B). Cells that are retained on the device remain trapped and viable after staining with calcein-AM, a viability dye. One striking observation from confocal scans of trapped cells is how cells deform into the traps and fully seal the trap (Fig. 3C).

We observe different capture efficiencies for each cell line with a characteristic band-stop response profile as a function of size (Fig. 3D). MCF7 cells (15.2 ± 3.6 μm, mode ± s.d.) were trapped at the highest rate, with a measured capture rate of 45.7 ± 4.4%. In contrast, the smaller Ramos (8.9 ± 1.5 μm) and HL60 cells (10.5 ± 2.3 μm), mimicking smaller leukocytes, were not captured at all (0%, n = 3 independent replicates). The largest cells, MDA-MB-231 (17.8 ± 3.4 μm), mimicking monocyte-sized cells, showed a reduced capture rate (1.7 ± 1.0%). Plotting these as a function of cell size yields a clear bandpass profile: HL60 points lie well below the cut-on (no trapping), MCF7 falls within the high-capture band, and MDA-MB-231 lies on the descending edge of the cut-off. The cell-based capture curve closely mirrors the microsphere-derived response but with a uniformly lower efficiency, the peak capture fraction for live cells is lower than for rigid beads. This reduction is largely attributable to the partial overlap between the band-stop capture efficiency profile (derived from bead measurements) and the modal size distributions of the cell lines. For example, MCF7 cells, which have the closest size match to the predicted high-efficiency region, still exhibit a broad size distribution with a substantial fraction of the population falling outside the band-stop region. As expected for a band-stop architecture, smaller leukocyte-sized lines (Ramos, HL60) fall below the cut-on and are intentionally rejected, which is beneficial for purity. MDA-MB-231 cells have only limited overlap with the predicted capture window, sitting on the descending edge, reducing their apparent capture efficiency. Additional factors likely exacerbate these effects, such as deformation-assisted escape – some cells that are nominally within the target size

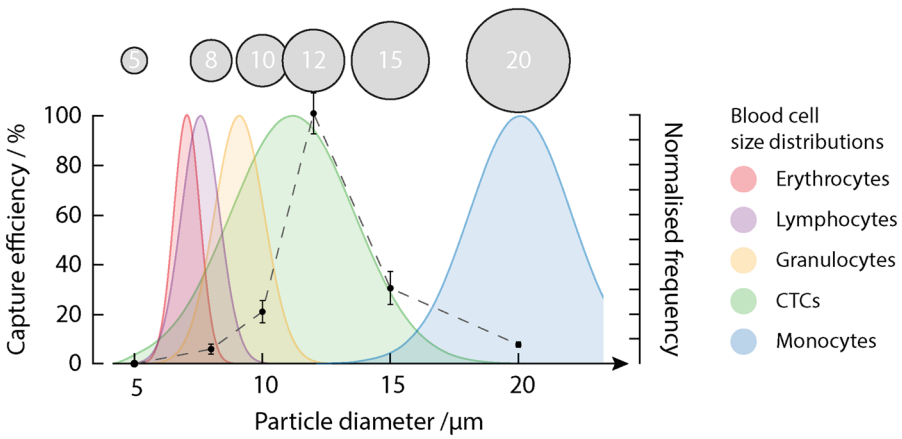

Fig. 2 Measuring the band-stop response with rigid microspheres. Polystyrene microspheres of defined diameters (5–20 μm, symbols at top) were perfused through the device at a constant flow rate. Capture efficiency was defined as the fraction of particles retained in the trap array. Points show mean ± s.d. for n = 3 independent runs per size; the dashed line is a spline through the bead means and represents the response function to rigid particles, establishing a characteristic band-stop filter profile. For reference, frequency normalised distributions of the diameter of major blood cell populations (erythrocytes, lymphocytes, granulocytes, monocytes) and of circulating tumour cells (CTCs) are overlaid (coloured curves; right y-axis). The device exhibits a pronounced band-stop centred in the CTC size range, while capture is suppressed for sizes corresponding to the bulk of leukocytes, particularly monocytes, indicating intrinsic selectivity for CTC-like dimensions under these hydrodynamic conditions.

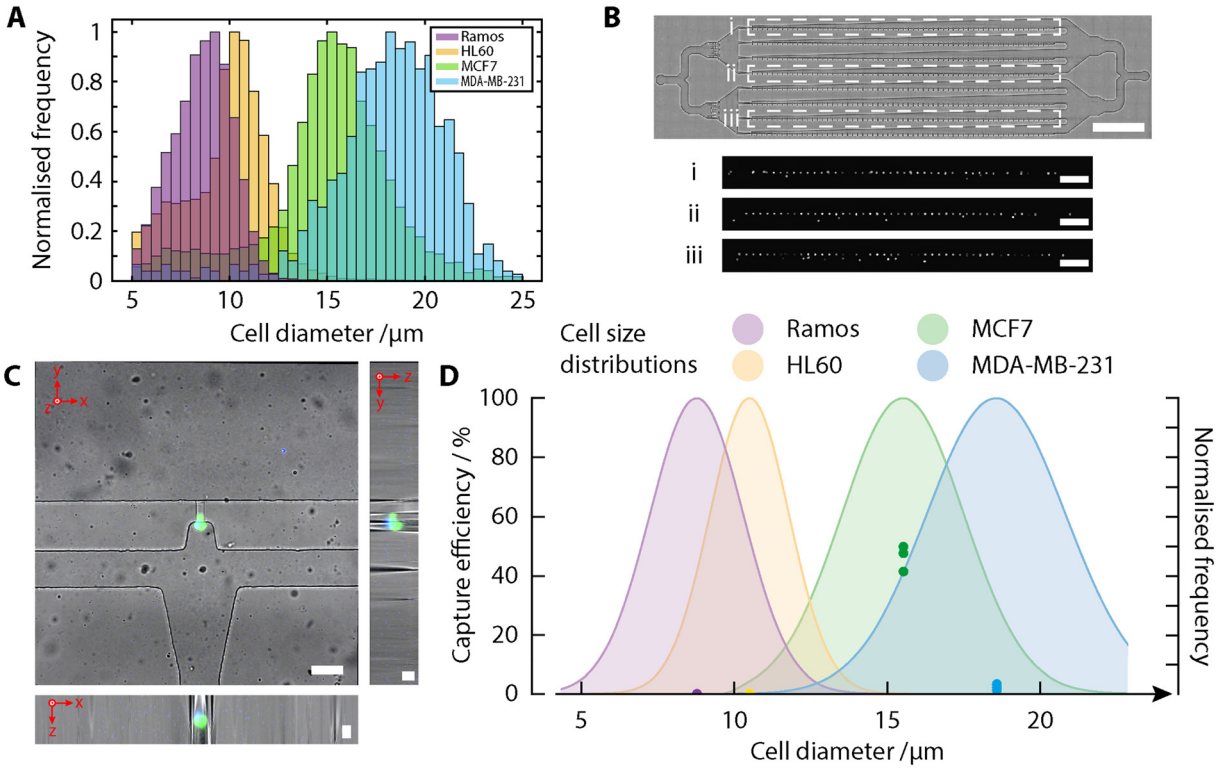

Fig. 3 Band-stopping cultured cancer cells. (A) Normalised distributions of single-cell diameters for four lines, chosen to span the band-stop filter. The mass of these distributions falls below, within and above the band-stop, as measured by microspheres. (B) Bright-field image of the microfluidic band-stop device showing the trapping array (flow from left to right). Scale bar, 5 mm. Insets i–iii: fluorescent images of cells arrayed in traps and retained on-chip after staining with calcein-AM, a viability dye. To visualise cells at this field of view, fluorescence images were morphologically dilated (see Experimental methods); individual cells are therefore intentionally shown larger than their true size. Scale bars, 2 mm. (C) Confocal orthogonal views of a single viable cell retained within a trap. The cell is stained with nuclear (blue, Hoechst 33394) and cytoplasm/viability (green, calcein-AM) dyes. The cell deforms into the trap and remains in place under flow. Scale bars: *xy* plane, 50 μm; *xz* and *yz* planes, 10 μm. (D) Whole-chip capture efficiency for each cell line tested (n = 3 independent runs per line). Data points (circles) are plotted at that line's modal diameter. Coloured curves show the corresponding normalised frequency distributions of single-cell diameter to indicate how each population samples the size-dependent response. The device preserves a clear band-stop profile for live cells, albeit with a lower capture efficiency than for rigid microspheres, consistent with deformation-assisted passage. Cell line/modelled blood analogue: Ramos/lymphocytes; HL-60/granulocytes; MCF-7/CTCs; MDA-MB-231/monocytes.

range can squeeze through or around traps where an equivalent rigid particle would have been retained. In other words, cell deformability effectively shifts the operational bandpass slightly, causing a fraction of would-be-captured cells to escape.

The decline in capture beyond the cut-off size is steeper for cells than for beads. We expect this is due to cells deforming and sealing traps completely, preventing additional captures (Fig. 3C). A highly deformable cell can behave as if it were effectively smaller in this context. We infer this is why a small fraction of the HL60 population, which has a trailing end of larger cells, still failed to trap; those HL60 cells likely deform and slip through where a rigid sphere of equal size might have been captured. In other words, deformation provides an escape mechanism for cells at the lower edge of the stop-band. Similarly, for the upper edge, a cell slightly above the cutoff diameter might still enter a trap if it can deform enough to fit the hydrodynamic streamlines into the side channel. However, once in the trap, such a cell will elongate and fully block the channel. In contrast, we expect that if a very deformable tumour cell (*e.g.* a highly mesenchymal CTC) were present and slightly oversized, it might transiently lodge and then slip out under flow. This would manifest as a potential "missed" capture. Our data with the mesenchymal MDA-MB-231 line hints at this.

While cell deformability is clearly a factor influencing microfluidic trapping, particularly in comparison to rigid beads, it cannot alone account for the observed bandpass capture profile. Instead, the selectivity window reflects an interplay between elastic compliance, hydrodynamic factors, and intercellular heterogeneity. The resulting capture rates are shaped not only by intrinsic mechanical properties but also by the geometry- and flow-dependent probability that a cell of given size and stiffness reaches and is retained within the trap.

We note that estimation of input cell number *via* suspension concentration and volumetric transfer introduces an inherent uncertainty, which becomes increasingly significant at low cell numbers. This arises from the precision of cell counting, pipetting of small volumes, and stochastic sampling effects (Poisson statistics) when drawing from dilute cell suspensions.

As a result, the true number of cells entering the device may deviate from the nominal input, particularly in experiments involving 10s–100s of cells or fewer. We mitigate these effects through replicate measurements and by focusing on capture efficiency and relative trends across conditions, which are robust to moderate uncertainty in absolute input number. Nonetheless, this limitation should be considered when interpreting experiments at the lowest input levels.

Band-stop capture from whole blood

We proceeded to evaluate the performance of the band-stop device when processing blood samples. Cells (pre-stained for viability) were spiked into 7.5 mL fresh, human whole blood samples at full haematocrit from healthy volunteers and processed by the device (Fig. 4A). The results paralleled the culture medium experiments (Fig. 4B); MCF7 cells were captured at the highest efficiency (38.7 ± 4.0%), Ramos and HL60 cells were entirely absent from traps (0% across all $n = 3$ independent replicates detected), and MDA-MB-231 cells showed intermediate capture (11.5 ± 4.6%). These demonstrate that despite the complex rheology of whole blood, the band-stop behaviour is preserved for this high-density clinical matrix. The small leukocyte-sized cells used here as controls still pass through as intended, whereas target-sized cells are retained, and oversized cells are largely excluded. Importantly, no clogging or channel fouling was observed even when processing millilitre-scale volumes of undiluted blood – trapped cells remained in place without being dislodged by shear, and non-target blood cells did not accumulate in the device. We attribute this to cells fully sealing traps and the sink providing a low-resistance bypass. Visual inspection during flow showed single cancer cells securely lodged in their traps surrounded by erythrocytes (Fig. 4A), underscoring that the selectivity is maintained under full haematocrit conditions. We did not detect trapping of intrinsic blood cells such as erythrocytes or either small (lymphocytes and granulocytes) or large (monocytes) white blood cells.

Parsortix reported capture rates of 54.7–58.7% for spiked MCF7 cells under typical operating conditions, marginally higher than those reported here.[24] The MyCTC chip reports higher apparent capture (~98%) but, critically, the capture fraction is flat across several cell lines whose single-cell diameters span ~10–30 μm.[34] This diameter-independent behaviour is characteristic of a simple low-pass architecture (single cut-on), in contrast to the band-stop profile measured here, which exhibits a peaked response with suppression below and above the stop-band. In terms of design, the MyCTC chip

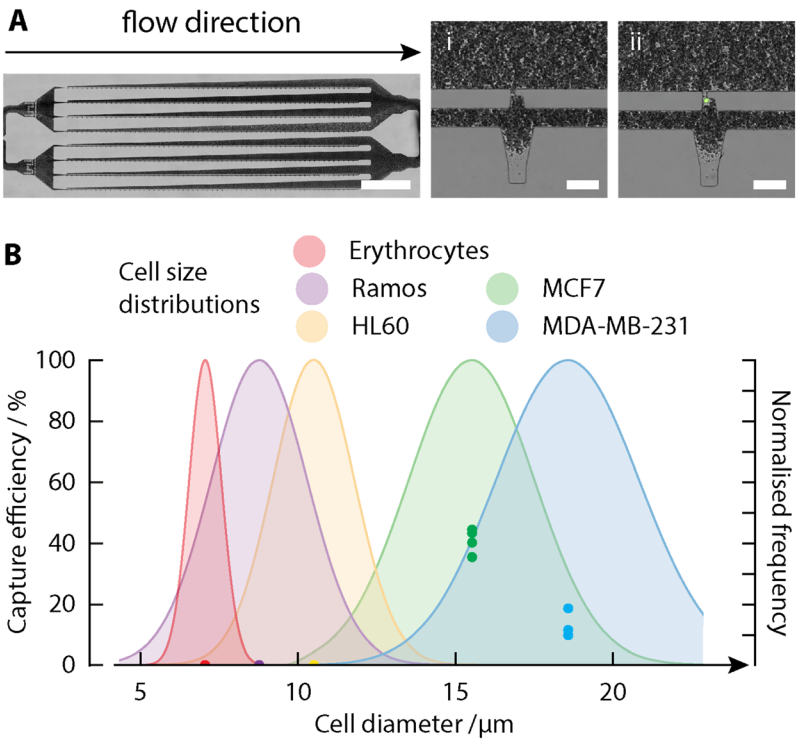

Fig. 4 Band-stopping of cancer cells spiked into whole blood. (A) Brightfield image showing unprocessed, anti-coagulated whole blood spiked with cultured cells being flowed through the microfluidic band-stop device (flow direction indicated). Scale bar, 5 mm. Insets: (i) empty trap and (ii) trap containing a single captured cell in the presence of a high density of blood cells. Scale bars, 100 μm. (B) Whole-chip capture efficiencies for model cell lines spiked into blood ($n = 4$ independent runs per line). Data points (circles) are plotted at that line's modal diameter with the normalised frequency distributions of their diameters overlaid on the graph. The band-stop profile is preserved for cells in blood, with capture efficiencies comparable to those measured for cells in culture medium, indicating that high haematocrit and co-flowing erythrocytes do not abolish the size-selective response. No leukocyte retention or channel obstruction was observed across any whole-blood experiments.

closely resembles Parsortix in its size/deformability gating and adds on-chip reservoirs to enable short-term culture and drug challenges. With respect to purity, issues with WBC contamination have been widely noted for low-pass systems. From the CTC : WBC ratios reported for MyCTC (~0.5–1.2) and the stated capture fractions, the implied WBC contamination is on the order of 10^3 WBCs per mL processed, comparable to Parsortix under similar conditions. In contrast, in our band-stop device no intrinsic blood cells (erythrocytes, lymphocytes/granulocytes, or monocytes) were detected in traps, consistent with a transfer function that suppresses capture both below and above the band-stop window.

To further test this, we proceeded to process unspiked blood samples (n = 3). For these sets of experiments, unprocessed blood samples were incubated with nuclear (Hoechst 33342) and viability dyes (calcein AM) to stain all platelets and WBCs present. After processing samples, images of the chip were acquired (bright-field and fluorescence) and analysed to enumerate cells. We did not observe any trapping of blood cells in cell traps from unspiked samples, confirming that those cells either bypassed the traps entirely or squeezed through without stopping. Blood cells are known to undergo extreme deformation in capillaries; in our device, any blood cell that did enter a trap would similarly deform and traverse it, which is likely why even outlier large WBCs did not remain lodged. Although no leukocytes were detected by whole-chip fluorescence imaging under the conditions tested, orthogonal downstream analyses, such as immunophenotyping or genomic assays on recovered fractions, will be required to define the lower limit of residual blood-cell carryover with greater sensitivity. Avoiding WBC contamination is advantageous for accurate downstream molecular profiling. Strategies to further purify CTCs are possible but minimising processing steps can avoid cell transfer losses and help simplify workflows.

No catastrophic failures, such as permanent clogging of the main channel, were encountered, even when a trap is occupied. The main and sink channels continue to carry flow, so subsequent samples can still pass. In rare cases, we noted fluorescent debris or platelets in a trap, but these did not accumulate systematically. On occasion, large clusters of cells (either bead doublets or naturally occurring cell clumps) were observed to bypass traps entirely, being too large to enter the side channels. Cell clusters, if present, are mostly diverted down the main channel and out to waste rather than clogging a trap. While our device is not aimed at cluster capture, this behaviour is beneficial for maintaining flow. It is noteworthy that other methods often struggle with cell aggregates (*e.g.* filters clog, DLD arrays jam); a band-stop system inherently deflects oversized debris or clusters and helps to preserve throughput.

Taken together across all cases (beads, cells in medium and cells spiked into whole blood), these results demonstrate a consistent behaviour where the microfluidic device acts as a band-stop filter: minimal trapping of smaller species below a cut-on diameter, maximal trapping in a band-stop range, and suppressed trapping again for larger objects above the cut-off diameter.

Reported processing rates for size- and deformability-based CTC platforms vary widely depending on operating mode and sample handling. For example, the Parsortix system is often quoted at manufacturer-reported flow rates of ~5 mL h^{-1} (or ~80 μL min^{-1}); however, literature reports indicate that processing a standard 7.5 mL blood sample typically requires ~4 h, corresponding to an effective average flow rate of ~30 μL min^{-1}.[35] Additional downstream steps, such as DEPArray-based single-cell isolation, will further extend total workflow times. Other passive microfluidic systems have reported much higher nominal flow rates (30 mL h^{-1} or ~500 μL min^{-1}), but these generally rely on dilution and pre-processing, or operate under conditions that compromise cell viability.[36] In this context, the operating range we report for our device (5–25 μL min^{-1}) is comparable to clinically used deformability-based systems when normalised for whole-blood processing. At the upper end of this range, 7.5 mL samples are processed in ~5 h, similar to Parsortix. Ideally, this would be shorter, and it is worth noting that our system processes undiluted, full haematocrit with significantly improved purity (no detectable leukocyte carryover) and preserved viability suitable for downstream functional assays. Lower flow rates extend processing times but were selected to ensure stable band-stop selectivity and gentle hydrodynamics. Importantly, the band-stop architecture is structurally well suited to parallelisation, as capture selectivity is governed locally by trap geometry rather than global flow conditions. We expect that throughput could be scaled linearly by increasing the number of parallel channels within a single device or by distributing samples across many multiplexed chips. Advances in multilayer microfabrication further support this strategy. For example, Chu *et al.* reported stacked channel architectures, where they demonstrate a device with 32 stacked microfluidic layers.[37] Parallelisation and multilayer implementations represent plausible routes to improved throughput in future work; however, how band-stop selectivity scales with these architectures remains to be determined.

Recovery of cells off-chip

After trapping and isolation, a key performance metric is how many cells can be recovered intact from the device. We investigated the release efficiency and cell recovery of the band-stop device (Fig. 5). We exploited the deformability of cells under relatively high flow rates to expel cells from the hydrodynamic traps, which transit the sink channels and are collected off-chip for further processing. After whole blood was infused, channels were gently flushed (5 μL min^{-1} for 5 min, or until the channels were observed to be cleared of erythrocytes) with culture medium to wash away non-retained cells followed by a brief, controlled high-flow pulse of culture medium (2.5 mL min^{-1} for 20 s) to eject trapped cells *via* the sink for collection (Fig. 5A and B).

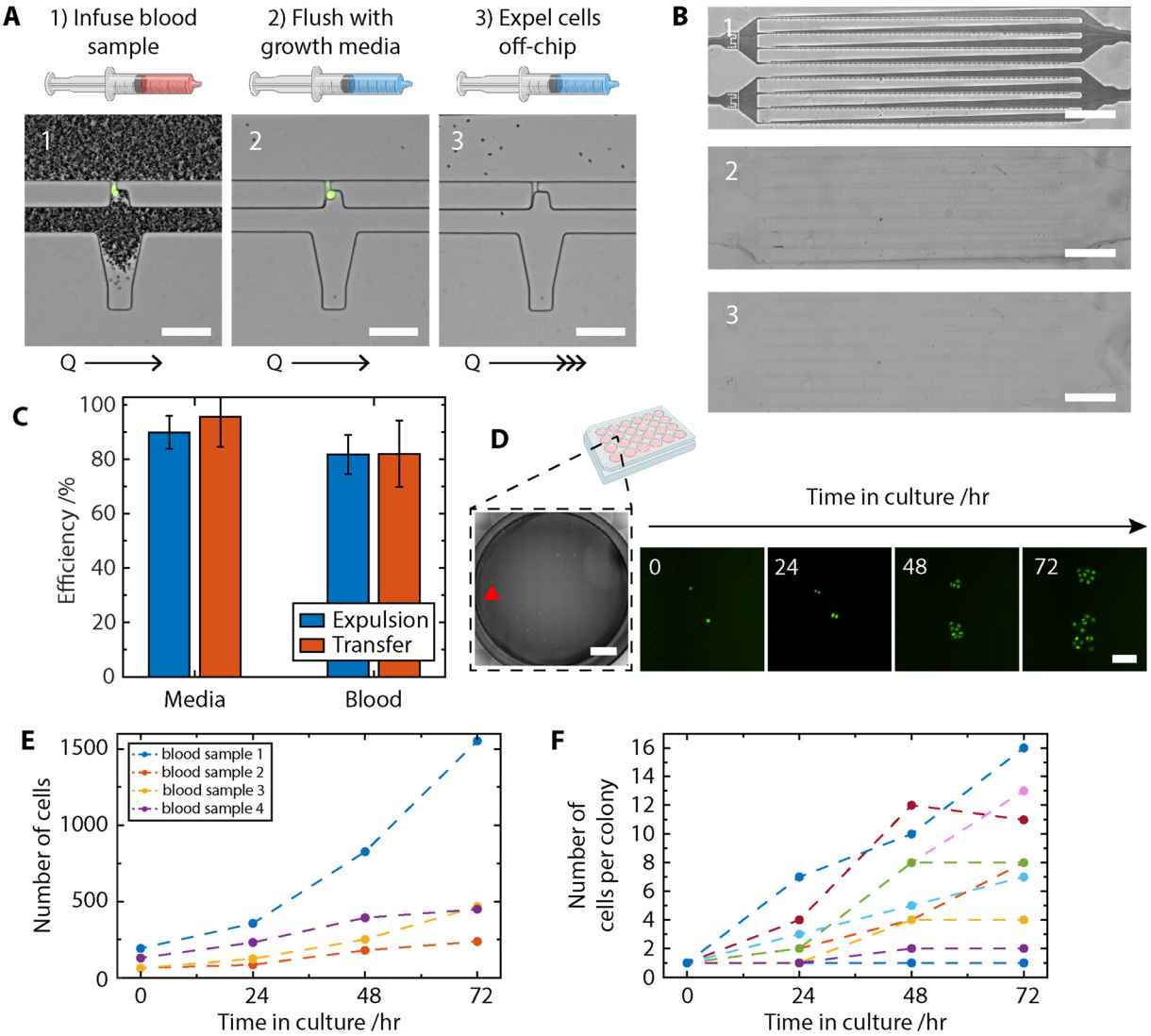

Fig. 5 Off-chip recovery of viable cells from the band-stop device. (A) The workflow for enrichment and recovery: (1) spiked whole blood is infused and processed through the trapping array. (2) Channels are gently flushed with growth medium to wash away non-retained cells while keeping trapped cells in place. (3) Trapped cells are expelled for collection by applying a brief high-flow pulse to squeeze cells through traps. Scale bars, 100 μm. (B) Whole-device bright-field images of the same chip (1) before and (2) after the flushing and (3) expulsions steps, illustrating the clearance of channels and release of retained cells. Scale bars, 5 mm. (C) Quantification of the expulsion efficiency (fraction of on-chip retained cells released from traps) and transfer efficiency (fraction of released cells delivered to the collection vessel off-chip) for samples run in culture medium and in whole blood (mean ± s.d., n = 3). Efficiencies are determined from whole-chip images acquired after each stage and whole-well scans after transfer. (D) The recovered product is directly transferred from the chip into the well of a 24-well plate *via* fluidic tubing. A representative whole-well image and time-lapse show viable cells proliferating after recovery. The time in culture is indicated in the number of hours (0–72 h) after transfer from the band-stop microfluidic device. To aid visualisation of cells in the whole-well image only, fluorescence masks are morphologically dilated (see Experimental methods). Scale bars: whole well, 2.5 mm; cropped cell fields, 100 μm. (E) Total number of recovered cells per well as a function of time in culture for independent blood samples. (F) Single-cell-derived colony growth trajectories from a representative experiment (10 randomly selected colonies), illustrating the heterogeneity in expansion dynamics – colonies may undergo rapid growth, delayed growth with a plateau, or persist as single viable cells over the same interval.

We quantified two stages of recovery: (1) an expulsion efficiency, *i.e.* the fraction of trapped cells that are successfully dislodged from traps by the release flow, and (2) a transfer efficiency, *i.e.* the fraction of expelled cells that are collected downstream in a well. Defining these two efficiencies helps us distinguish between our ability to expel cells within the chip and also any losses from chip-to-world interfaces and off-chip tubing.

We achieved an expulsion of 89.9 ± 6.1% of trapped MCF7 cells for cells isolated from simple medium and 81.8 ± 7.2% for MCF7 spiked in blood. The slightly lower expulsion rate in blood experiments may be due to occasional cell debris or fibrin in blood providing mild adhesion, evident by semi-transparent strings in channels. Once expelled, cells travel through outlet tubing into a well plate for collection. We recovered 95.6 ± 11.1% of the

expelled cells in medium and 82.0 ± 12.3% in the blood case. In comparison, the Parsortix harvest rate (number of cells eluted from the system onto a slide) has been reported to be 44.8 ± 4.5%.[24] Losses in this transfer step can arise from cells sticking to tubing or settling in dead volumes; the somewhat reduced transfer from the blood runs could indicate that the presence of serum proteins or minor clots made cells a bit "stickier" during transit. This may be improved by optimising surface coatings on tubing or assessing the line for dead volumes. Nonetheless, a majority of the initially trapped cells were ultimately retrieved, which is an encouraging result for a purely physical capture mechanism with no further intervention. Importantly, the cells that were recovered were viable, as confirmed by culturing and live/dead staining (Fig. 5D–F). The method of release, as opposed to, *e.g.* enzymatic detachment, likely helps preserve cell integrity. The recovered cells readily reattached in culture and proliferated over 72 h, showing no overt signs of damage from the trapping or release process (Fig. 5D).

We observed some carryover of erythrocytes into collection wells but no WBCs. After cells attached, erythrocytes could be readily removed by gentle washes with medium. We observed no change in proliferation capacity whether erythrocytes were present in wells or not. Recovered cells expanded 5.6 ± 2.4-fold over 72 h in culture (Fig. 5E). We observed single-cell-derived colony growth from each recovery (Fig. 5D and F), where colonies were observed to undergo rapid growth, delayed growth with a plateau or persist as single viable cells over the time in culture. To our knowledge, such expansion of CTC analogues directly from an undiluted blood sample without any immunoselection or subsequent purge of WBCs is unprecedented, and it highlights a key advantage of a band-stop approach.

On-chip drug response *vs.* standard culture

The drug sensitivity of MCF7 breast cancer cells on the microfluidic chip was found to be comparable to that in conventional off-chip culture. (Fig. 6). MCF7 cells enriched and

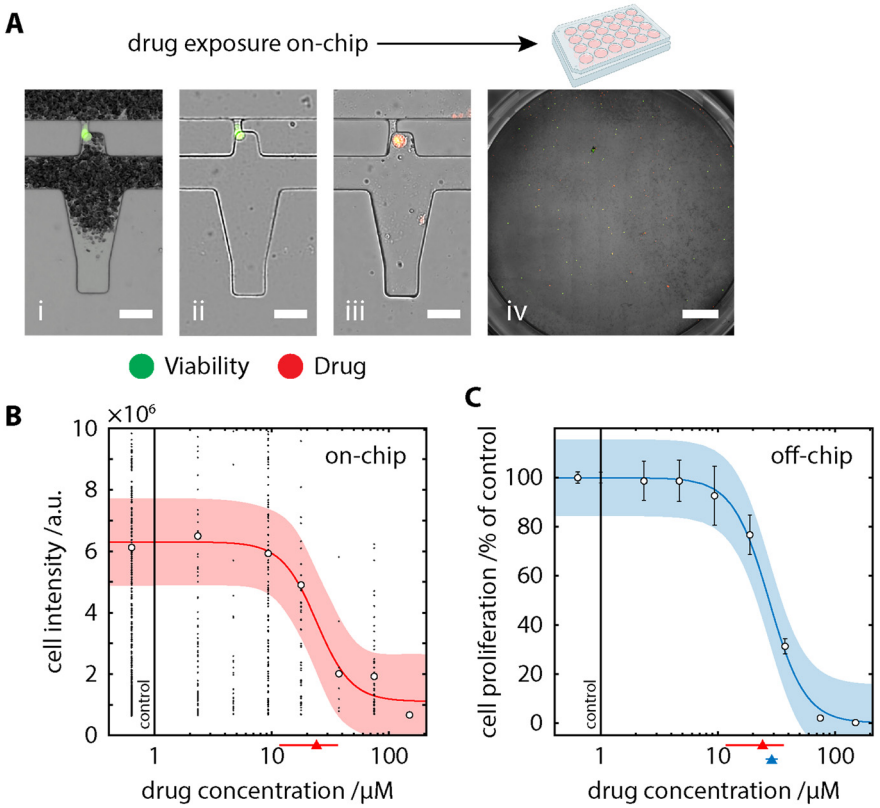

Fig. 6 On-chip drug response of enriched cancer cells. (A) Workflow for on-chip drug exposure prior to recovery. (i) Cells are first isolated from whole blood in the band-stop array (green indicates calcein-AM staining for viability). (ii) Devices are then gently perfused with growth medium containing the test compound at a defined concentration. (iii) Cells are maintained on-chip for 24 h in drug. Doxorubicin's intrinsic red fluorescence confirms cellular uptake (orange/red overlay). (iv) After exposure, cells are expelled from the traps and transferred directly to multiwell plates for downstream assays. At this field of view, individual cells are not resolvable; to aid visualisation, fluorescence masks are morphologically dilated (see Experimental methods). Scale bars: (i–iii) 50 μm, (iv) 2 mm. (B) On-chip dose–response curve for 24 h doxorubicin exposure, quantified as single-cell viability dye intensity. (C) Off-chip dose–response curve, quantified as survival at 24 h. In both cases, data are fit with a four-parameter logistic model (solid lines, red and blue) with 90% confidence intervals (shaded regions). IC_{50} values are indicated by triangles, with horizontal lines spanning the confidence interval. The comparable IC_{50}s indicate that on-chip maintenance and drug delivery preserve pharmacological sensitivity while enabling an integrated enrichment-assay workflow.

retained in the band-stop array were exposed under perfusion (24 h) to doxorubicin and their response quantified by a single-cell viability readout (Fig. 6A). Matched off-chip assays that used the same exposure and endpoint were also conducted. Dose–response curves were fitted to a four-parameter logistic model with IC_{50} estimated by non-linear least squares. The on-chip IC_{50} for doxorubicin was 24.2 μM (90% CI: 11.7–36.6 μM) (Fig. 6B) *versus* 28.9 μM off-chip (90% CI: 25.6–32.1 μM) (Fig. 6C). The overlapping confidence intervals indicate no statistically significant difference between the two conditions, suggesting that the microfluidic environment did not markedly alter the drug response. Importantly, the IC_{50} values measured here are in line with literature reports for MCF7 cell exposure to doxorubicin.[38–40] The single-cell fluorescence readouts in Fig. 6B exhibit substantial heterogeneity, which is characteristic of asynchronous cancer cell populations and is well documented for calcein-AM-based viability assays. Such variability may arise from differences in intracellular esterase activity, dye loading and efflux kinetics, metabolic state, and cell-cycle phase, all of which contribute to broad fluorescence distributions even in clonal cell lines such as MCF7. Drug response metrics were therefore extracted using population-level dose–response fitting.

Reported MCF7 IC_{50} values span $>10^2$-fold depending on exposure time, assay, and culture context. Our 24 h on-chip and off-chip values sit at the higher end of this broad range but are consistent with a short exposure window. This confirms that the on-chip assay yields reliable pharmacological readouts. Such a shift could be due to microenvironmental factors on the chip, such as cell confinement or shear stress, but overall, the drug efficacy on-chip mirrors that in standard 2D culture. This is an encouraging result, as it validates the use of the microfluidic platform for drug screening without introducing significant artifacts in cell sensitivity. Maintaining consistency in drug response is crucial because it means cells captured and tested on-chip remain representative of their true chemosensitivity. The chip-based assay required only a small number of cells yet produced a clear dose–response curve, underscoring the platform's suitability for scarce samples such as CTCs. It also suggests that drug exposure and nutrient conditions in the chip were adequate for the cells, avoiding issues such as excessive stress or quiescence that could otherwise skew drug susceptibility. Overall, the chip-based viability assay provided a robust measure of drug potency that is equivalent to conventional assays, validating the chip for downstream pharmacological evaluation of CTCs.

Landmark studies have shown that if CTCs can be expanded into stable cell lines or organoids, one can perform high-throughput drug screenings that sometimes correlate with patient clinical responses.[41] For instance, Yu *et al.* established long-term CTC cultures from breast cancer patients and identified drug sensitivities *in vitro* that aligned with the patients' treatment outcomes – a compelling demonstration of CTC-derived models for therapy guidance.[42] However, deriving permanent CTC cell lines remains exceedingly challenging and time-consuming, achieved only in a handful of cases. Therefore, microfluidic short-term assays fill an important gap by rapidly assessing drug efficacy on freshly harvested CTCs or a minimal expansion thereof.

Parsortix also provides label-free enrichment, but drug assays are performed off-device after release (often following short expansion), introducing additional handling time and potential selection. In contrast, the MyCTC chip integrates capture with on-chip short-term culture and parallel drug challenges, typically over 4–7 days, enabling multi-condition screening but implicitly altering cell number/state prior to testing and commonly reporting fixed-dose viability. In the context of these technologies, the band-stop chip's performance is highly encouraging. It combines the strengths of viable cell capture with immediate on-chip drug testing that yields quantitative results consistent with conventional assays while preserving compatibility with subsequent recovery for molecular or longer-term functional studies. A major advantage of an integrated approach is speed and fidelity. By minimising manipulation, we reduce cell losses and avoid phenotypic drift that can occur during prolonged culture.

Conclusions

We have reported a microfluidic band-stop filter that implements a size-selective transfer function with explicit cut-on and cut-off bounds so that only cells within a designed window are retained, whereas both smaller and larger cells pass. Across rigid calibrants, cultured lines in medium, and spiked whole blood, the device exhibits a band-stop profile: a sharp rise at the lower edge, a finite high-capture plateau, and suppression at larger diameters. This response is preserved under high haematocrit, establishing band-stopping as a robust, label-free route to viable CTC enrichment. Notably, no leukocyte capture was detected in unspiked whole-blood runs by whole-chip imaging under our operating conditions, addressing a long-standing purity limitation of size-based methods while maintaining gentle hydrodynamics compatible with live-cell work.

A wide range of microfluidic strategies for CTC isolation have been reported over the past decade, including immunoaffinity capture, inertial and spiral microchannels, deterministic lateral displacement, hydrodynamic filtering, and hybrid approaches, each with distinct trade-offs between recovery, purity, throughput, and cell viability. Comprehensive reviews of these technologies consistently highlight that most size- and deformability-based devices operate as effective low-pass filters, enriching larger cells at the cost of substantial leukocyte co-capture and limited suitability for downstream functional assays, particularly in undiluted whole blood. High-throughput platforms such as spiral inertial devices or the CTC-iChip achieve impressive recovery and depletion, but typically rely on dilution, pre-processing, or multi-stage workflows that complicate integration with live-cell assays. Conversely, clinical

systems such as Parsortix retain a broad range of cell sizes, resulting in well-documented leukocyte contamination.

In this context, the present work introduces a fundamentally different band-stop operating principle that defines both lower and upper size bounds for capture. This bounded transfer function enables selective retention of CTC-sized cells while excluding both smaller leukocytes and larger non-target cells, achieving high purity directly from undiluted whole blood without clogging or pre-processing. Importantly, this selectivity is achieved in a format compatible with prolonged on-chip cell maintenance and pharmacological interrogation, capabilities that are not generally accessible with existing size-based microfluidic platforms. The band-stop architecture therefore complements high-throughput or threshold-based systems, offering a distinct niche where purity, viability, and functional readouts are prioritised.

While the present study does not include a full parametric sweep of flow rate or concentration, operating conditions were deliberately chosen to reflect clinically relevant whole-blood processing while preserving cell viability and stable band-stop selectivity. Under these conditions, recovery, purity, and viability metrics were reproducible across independent runs, and no clogging or degradation of performance was observed. Systematic lifetime testing, long-duration operation, and expanded parameter optimisation represent important directions for future translational studies but fall beyond the scope of this work, which focuses on establishing the band-stop mechanism and demonstrating its compatibility with viable downstream assays. While the present study establishes the band-stop principle experimentally, future work could incorporate computational fluid dynamics, streamline analysis, and particle trajectory modelling to quantify hydrodynamic admission, trap occupancy, and size-dependent transport in greater detail and to guide design optimisation.

As with all physical enrichment strategies, the band-stop architecture introduces an explicit selection bias, in this case defined by cell size and deformability. While this necessarily excludes some CTCs that fall outside the engineered window, the trade-off is deliberate: restricting capture to a bounded population enables high purity, minimal leukocyte carryover, and reliable downstream functional assays. Importantly, the band-stop window is geometrically tuneable, potentially allowing adaptation to different tumour types or disease stages, and could be applied sequentially or in parallel to sample broader phenotypic space. The clinical implications of this selectivity will ultimately require focused evaluation using patient-derived samples, including systematic interrogation of the phenotypes of cells both retained on-chip and those that transit the device. Such studies will be essential to determine how the engineered size window maps onto clinically relevant CTC subpopulations and therapeutic response. While widening the band-stop window would be expected to increase CTC recovery, this would inevitably occur at the expense of increased leukocyte contamination, underscoring the central trade-off between breadth of capture and assay purity. Defining the optimal balance between these competing requirements represents an important direction for future translational studies.

Functionally, the platform closes the gap between enrichment and assay. Cells retained in traps withstand buffer exchange and continuous perfusion drug exposure, enabling on-device dose response measurements from low inputs. For MCF7 cells, on-chip 24 h doxorubicin IC_{50} values were statistically concordant with matched off-chip culture, indicating that hydrodynamic admission and confinement do not distort pharmacological sensitivity. Trapped cells are recoverable on demand by a brief high-flow pulse and remain viable for off-chip expansion, supporting downstream molecular analyses. Together, these capabilities move liquid biopsy beyond enumeration toward quantitative, functional testing on freshly enriched cells without transfer-induced losses or expansion-related selection.

Conceptually, band-stopping reframes label-free CTC enrichment as an engineered transfer function that can be modelled, fitted, and quality-controlled across devices and runs. Practically, the architecture affords high purity in undiluted blood, immediate assay ability on the captured material, and parametric retuning to target alternative rare-cell phenotypes or disease contexts. These attributes make the approach complementary to high-throughput or expansion-based systems where rapid, low-N, decision-oriented pharmacology is required.[43] With these advances and prospective testing on patient samples, band-stop microfluidics can mature into a practical, precision-medicine tool that prioritises purity and cell health to support downstream, actionable clinical decision-making and therapy selection.

Experimental methods

Microfluidic device

Fabrication. Devices were fabricated by standard soft lithography in PDMS (Sylgard 184, Dow Corning). Pre-polymer and curing agent (10 : 1) were mixed, degassed, cast on SU-8 masters, and cured at 75 °C (≥12 h). PDMS slabs were peeled, access ports drilled (0.6 mm), cleaned in 70% ethanol, dried under N_2, and plasma-bonded to glass (room-air plasma, 200 W, 60 s; Diener, Germany). Bonded chips were post-baked at 75 °C for 3 h to strengthen adhesion.

Design. Each chip comprised 8 parallel main channels (50 μm × 30.25 mm × 30 μm; $W \times L \times H$), with 60 traps at 500 μm pitch along each channel. Traps consisted of a cell-park (isosceles trapezoid, 30–40 μm × 30 μm × 30 μm; $W \times L \times H$) and a hydrodynamic trap (10.0 ± 1.0 μm × 20 μm × 10 μm; $W \times L \times H$). Sink channels (30 μm height) ran parallel, widening from 100 μm at the first to 900 μm at the last trap. The inlet bifurcated into filtration channels and then into two banks of four main channels; downstream termini rejoined their sink channels and merged at the outlet. Upstream debris filters comprised a 50 μm "sieve" followed by a 26 μm barrier.

Preparation. Prior to use, chips were vacuum primed with PBS for 20 min to fully wet the channel network, then connected to syringe pumps (KD Scientific) *via* Tygon tubing (510 μm ID, 1/16″OD). Unless stated otherwise, sample perfusion ranged from 5 to 25 μL min^{-1}.

Image acquisition and analysis

All imaging used an inverted microscope (Nikon Ti2; Nikon, Japan) with a motorised XY-stage for whole-array tiling. For image analysis, whole-device mosaics were cropped by channel and segmented in Fiji/ImageJ using StarDist 2D.[44,45] ROIs were manually screened to discriminate cells. Capture counts were derived from bright-field/fluorescence overlays (calcein-AM/Hoechst 33342 masks). For figure visualisation where indicated only, fluorescence mosaics (whole-chip and whole-well) were morphologically dilated using a 5 × 5 structuring element to enhance the visibility of cell locations at very large fields of view. Dilation increases the bright mask area (and thus the apparent cell size) but was not applied to any images used for quantification; all analyses were performed on the original non-dilated data.

Bead experiments

Polystyrene microspheres (nominal diameters 5, 8, 10, 12, 15, 20 μm; Fluka) were mixed for 5 min then perfused at 5 μL min^{-1}. To discourage aggregation, suspensions were prepared in 2% (w/v) sodium dodecyl sulphate solution. Whole-array bright-field images were acquired and retained beads counted. Capture efficiency was calculated as the fraction of the nominal input retained in the trap array.

Cell experiments

Cell culture and preparation. All cell lines (ATCC) were maintained at 37 °C, 5% CO_2, 95% relative humidity in DMEM supplemented with FBS, L-glutamine, and penicillin/streptomycin. Cells were passaged 2–3 times per week (1 : 10). Adherent lines were detached with trypsin/EDTA, triturated to single cells, and, where indicated, stained. Suspension cells required no detachment and were passaged by dilution.

Human samples. Healthy volunteer whole blood samples were obtained. Blood (7.5 mL) was collected in BD Vacutainer EDTA tubes and used within 3 h of draw. To match the 480-trap array capacity and avoid saturation, spike-in concentrations were selected such that ~480 tumour cells were introduced into the device per run. Institutional approvals and informed consent were obtained according to local policies. All blood-based spiking experiments were performed in undiluted, unprocessed whole blood at full haematocrit, with no dilution, erythrocyte lysis, or density pre-enrichment.

Ethics approval. Human samples used in this research project were obtained and all experiments were performed in accordance with the Guidelines of the Imperial College Healthcare Tissue Bank (ICHTB). ICHTB is supported by the National Institute for Health Research (NIHR) Biomedical Research Centre based at Imperial College Healthcare NHS Trust and Imperial College London. ICHTB is approved by Wales REC3 to release human material for research (17/WA/0161). Approvals were provided by the ethics committee from ICHTB and informed consent was obtained from all human participants of this study.

Size-distribution profiling. For single-cell diameter distributions, cells were stained with calcein-AM then dispensed into wells and allowed to settle for 25 min prior to imaging. Segmentation was performed in Fiji/ImageJ using StarDist 2D.[44,45] Object areas were converted to equivalent spherical diameters and compiled into distributions for each line.

Release and off-chip recovery. After assays or capture-only runs, unretained cells were washed out (5 μL min^{-1} of culture medium for 5 min, or until the channels are observed to be flushed of erythrocytes), then a brief high-flow pulse (2.5 mL min^{-1} for 20 s) expelled trapped cells through the throats into sink channels and out *via* outlet tubing to a 24-well plate. Expulsion efficiency was defined as the fraction of on-chip retained cells removed from traps by the pulse; transfer efficiency was the fraction of expelled cells recovered in the well. Efficiencies were quantified by whole-array imaging before/after expulsion and whole-well imaging after transfer.

On-chip drug exposure. Following capture, channels were gently exchanged with growth medium containing doxorubicin at defined concentrations and maintained for 24 h on-chip (37 °C, 5% CO_2). Doxorubicin uptake was confirmed by intrinsic red fluorescence. Imaging was performed immediately post-capture, post-exchange, and after 24 h. Viability readouts were derived from single-cell fluorescence intensity. Matched off-chip assays used identical exposure and endpoints.

Capture assays. For media runs, whole-array images acquired in bright-field and fluorescence channels using standard filters were used for enumeration. For blood runs, whole blood samples were spiked with the same nominal cell input and processed through the chip. Viability (calcein-AM) and nuclear (Hoechst 33342) dyes facilitated discrimination of spiked cells and intrinsic blood cells. In unspiked blood controls, whole blood samples were perfused at 5 μL min^{-1} and channels imaged to assess cell carry-over. Cells were first quantified using haemocytometer-based counting to obtain a bulk concentration. Aliquots corresponding to the desired nominal input were then prepared by volumetric transfer using calibrated pipettes. Immediately prior to loading, suspensions were gently mixed. For low-input experiments, where small volumes were required, care was taken to use appropriate pipetting ranges and replicate preparations to reduce volumetric error. Capture efficiency was calculated as the number of retained particles or cells divided by the nominal number introduced. For rigid bead experiments, values slightly above 100% reflect counting uncertainty and occasional multi-particle occupancy where incompletely sealing beads permit continued flow into a trap. Losses upstream of the chip can occur during long processing times, *e.g.* cell sedimentation in syringes and tubing. Strategies to minimise or avoid such losses have been reported.[46]

Data and statistical analysis

Unless stated, a minimum of $n = 3$ independent runs were conducted per condition. Data are reported as mean ± s.d. Dose–response curves were fitted to a four-parameter logistic model and IC_{50} estimates are reported with 90% confidence intervals obtained by profile-likelihood.

Author contributions

ASR conceived and designed the study and, with RCC and PD, secured funding. ASR, RCC, PD and SA supervised the project. LK performed the experiments and, together with ASR, analysed the data. ASR and LK drafted the manuscript; all authors revised and approved the final version. CRediT taxonomy as follows. Conceptualization: ASR. Funding acquisition: ASR, RCC, PD. Supervision: ASR, RCC, PD, SA. Investigation: LK. Formal analysis: LK, ASR. Methodology: ASR, LK, GN. Writing (original draft): LK, ASR. Writing (review & editing): LK, SA, RCC, PD, ASR.

Conflicts of interest

The authors declare no competing interests, or other interests that might be perceived to influence the results and/or discussion reported in this paper.

Data availability

All relevant data are available from the authors upon reasonable request.

Acknowledgements

This work was supported by a Community of Analytical Measurement Science Lectureship award and an Engineering and Physical Science Research Council (EPSRC) Innovation fellowship awarded to ASR. LK was supported by an EPSRC iCASE award to ASR, RCC and PD. Human samples used in this research project were obtained from the Imperial College Healthcare Tissue Bank (ICHTB). ICHTB is supported by the National Institute for Health Research (NIHR) Biomedical Research Centre based at Imperial College Healthcare NHS Trust and Imperial College London. ICHTB is approved by Wales REC3 to release human material for research (17/WA/0161). All authors acknowledge the NIHR Biomedical Facility at Imperial College London for infrastructure support. We thank Dr Laura Kenny for assistance with blood collection.

References

1 L. Descamps, D. Le Roy and A.-L. Deman, Microfluidic-Based Technologies for CTC Isolation: A Review of 10 Years of Intense Efforts towards Liquid Biopsy, *Int. J. Mol. Sci.*, 2022, **23**, 1981, DOI: 10.3390/ijms23041981.

2 G. Vona, *et al.*, Isolation by size of epithelial tumor cells : a new method for the immunomorphological and molecular characterization of circulatingtumor cells, *Am. J. Pathol.*, 2000, **156**, 57–63, DOI: 10.1016/S0002-9440(10)64706-2.

3 A. Toss, Z. Mu, S. Fernandez and M. Cristofanilli, CTC enumeration and characterization: moving toward personalized medicine, *Ann. Transl. Med.*, 2014, **2**, 108, DOI: 10.3978/j.issn.2305-5839.2014.09.06.

4 A. J. Rushton, G. Nteliopoulos, J. A. Shaw and R. C. Coombes, A Review of Circulating Tumour Cell Enrichment Technologies, *Cancers*, 2021, **13**, 970, DOI: 10.3390/cancers13050970.

5 M. Vidlarova, *et al.*, Recent Advances in Methods for Circulating Tumor Cell Detection, *Int. J. Mol. Sci.*, 2023, **24**, 3902, DOI: 10.3390/ijms24043902.

6 D. A. Smirnov, *et al.*, Global gene expression profiling of circulating tumor cells, *Cancer Res.*, 2005, **65**, 4993–4997, DOI: 10.1158/0008-5472.CAN-04-4330.

7 E. A. Punnoose, *et al.*, Molecular biomarker analyses using circulating tumor cells, *PLoS One*, 2010, **5**, e12517, DOI: 10.1371/journal.pone.0012517.

8 B. Mostert, *et al.*, Detection of circulating tumor cells in breast cancer may improve through enrichment with anti-CD146, *Breast Cancer Res. Treat.*, 2011, **127**, 33–41, DOI: 10.1007/s10549-010-0879-y.

9 S. A. Mani, *et al.*, The epithelial-mesenchymal transition generates cells with properties of stem cells, *Cell*, 2008, **133**, 704–715, DOI: 10.1016/j.cell.2008.03.027.

10 R. Kalluri and R. A. Weinberg, The basics of epithelial-mesenchymal transition, *J. Clin. Invest.*, 2009, **119**, 1420–1428, DOI: 10.1172/JCI39104.

11 H. Lin, M. Balic, S. Zheng, R. Datar and R. J. Cote, Disseminated and circulating tumor cells: Role in effective cancer management, *Crit. Rev. Oncol. Hematol.*, 2011, **77**, 1–11, DOI: 10.1016/j.critrevonc.2010.04.008.

12 M. E. Francart, *et al.*, Epithelial-mesenchymal plasticity and circulating tumor cells: Travel companions to metastases, *Dev. Dyn.*, 2018, **247**, 432–450, DOI: 10.1002/dvdy.24506.

13 K. C. Andree, G. van Dalum and L. W. Terstappen, Challenges in circulating tumor cell detection by the CellSearch system, *Mol. Oncol.*, 2016, **10**, 395–407, DOI: 10.1016/j.molonc.2015.12.002.

14 D. Wirtz, K. Konstantopoulos and P. C. Searson, The physics of cancer: the role of physical interactions and mechanical forces in metastasis, *Nat. Rev. Cancer*, 2011, **11**, 512–522, DOI: 10.1038/nrc3080.

15 Y. Lee, G. Guan and A. A. Bhagat, ClearCell(R) FX, a label-free microfluidics technology for enrichment of viable circulating tumor cells, *Cytometry, Part A*, 2018, **93**, 1251–1254, DOI: 10.1002/cyto.a.23507.

16 M. C. Miller, P. S. Robinson, C. Wagner and D. J. O'Shannessy, The Parsortix Cell Separation System-A versatile liquid biopsy platform, *Cytometry, Part A*, 2018, **93**, 1234–1239, DOI: 10.1002/cyto.a.23571.

17 E. Sollier-Christen, C. Renier, T. Kaplan, E. Kfir and S. C. Crouse, VTX-1 Liquid Biopsy System for Fully-Automated and Label-Free Isolation of Circulating Tumor Cells with Automated Enumeration by BioView Platform, *Cytometry, Part A*, 2018, **93**, 1240–1245, DOI: 10.1002/cyto.a.23592.

18 W. S. Low and W. A. Wan Abas, Benchtop technologies for circulating tumor cells separation based on biophysical properties, *BioMed Res. Int.*, 2015, **2015**, 239362, DOI: 10.1155/2015/239362.
19 P. A. J. Mendelaar, *et al.*, Defining the dimensions of circulating tumor cells in a large series of breast, prostate, colon, and bladder cancer patients, *Mol. Oncol.*, 2021, **15**, 116–125, DOI: 10.1002/1878-0261.12802.
20 F. Coumans, G. van Dalum and L. Terstappen, CTC Technologies and Tools, *Cytometry, Part A*, 2018, **93**, 1197–1201, DOI: 10.1002/cyto.a.23684.
21 J. Zhang, *et al.*, Fundamentals and applications of inertial microfluidics: a review, *Lab Chip*, 2016, **16**, 10–34, DOI: 10.1039/C5LC01159K.
22 W. S. Iv, C. D. Reyes and G. P. López, Microfluidic cell sorting: a review of the advances in the separation of cells from debulking to rare cell isolation, *Lab Chip*, 2015, **15**, 1230–1249, DOI: 10.1039/C4LC01246A.
23 H. Cho, *et al.*, Microfluidic technologies for circulating tumor cell isolation, *Analyst*, 2018, **143**, 2936–2970, DOI: 10.1039/C7AN01979C.
24 L. Xu, *et al.*, Optimization and Evaluation of a Novel Size Based Circulating Tumor Cell Isolation System, *PLoS One*, 2015, **10**, e0138032, DOI: 10.1371/journal.pone.0138032.
25 C. Poggiana, *et al.*, A model workflow for microfluidic enrichment and genetic analysis of circulating melanoma cells, *Sci. Rep.*, 2025, **15**, 15329, DOI: 10.1038/s41598-025-99153-y.
26 E. Ozkumur, *et al.*, Inertial focusing for tumor antigen-dependent and -independent sorting of rare circulating tumor cells, *Sci. Transl. Med.*, 2013, **5**, 179ra147, DOI: 10.1126/scitranslmed.3005616.
27 A. Mishra, *et al.*, Ultrahigh-throughput magnetic sorting of large blood volumes for epitope-agnostic isolation of circulating tumor cells, *Proc. Natl. Acad. Sci. U. S. A.*, 2020, **117**, 16839–16847, DOI: 10.1073/pnas.2006388117.
28 A. Mishra, *et al.*, Tumor cell-based liquid biopsy using high-throughput microfluidic enrichment of entire leukapheresis product, *Nat. Commun.*, 2025, **16**, 32, DOI: 10.1038/s41467-024-55140-x.
29 T. N. Fehm, *et al.*, Diagnostic leukapheresis for CTC analysis in breast cancer patients: CTC frequency, clinical experiences and recommendations for standardized reporting, *Cytometry, Part A*, 2018, **93**, 1213–1219, DOI: 10.1002/cyto.a.23669.
30 J. Zhai, *et al.*, Drug screening on digital microfluidics for cancer precision medicine, *Nat. Commun.*, 2024, **15**, 4363, DOI: 10.1038/s41467-024-48616-3.
31 J. P. Cieslik, *et al.*, Liquid Biopsy in Metastatic Breast Cancer: Path to Personalized Medicine, *Oncol. Res. Treat.*, 2025, 1–15, DOI: 10.1159/000545643.
32 W.-H. Tan and S. Takeuchi, A trap-and-release integrated microfluidic system for dynamic microarray applications, *Proc. Natl. Acad. Sci. U. S. A.*, 2007, **104**, 1146–1151, DOI: 10.1073/pnas.0606625104.
33 M. Yamada and M. Seki, Hydrodynamic filtration for on-chip particle concentration and classification utilizing microfluidics, *Lab Chip*, 2005, **5**, 1233–1239, DOI: 10.1039/B509386D.
34 F. D. Schwab, *et al.*, MyCTC chip: microfluidic-based drug screen with patient-derived tumour cells from liquid biopsies, *Microsyst. Nanoeng.*, 2022, **8**, 130, DOI: 10.1038/s41378-022-00467-y.
35 A. Meunier, *et al.*, Gravity-based microfiltration reveals unexpected prevalence of circulating tumor cell clusters in ovarian and colorectal cancer, *Commun. Med.*, 2025, **5**, 33, DOI: 10.1038/s43856-024-00702-9.
36 J. F. Edd, *et al.*, Microfluidic concentration and separation of circulating tumor cell clusters from large blood volumes, *Lab Chip*, 2020, **20**, 558–567, DOI: 10.1039/C9LC01122F.
37 C.-H. Chu, *et al.*, Hybrid negative enrichment of circulating tumor cells from whole blood in a 3D-printed monolithic device, *Lab Chip*, 2019, **19**, 3427–3437, DOI: 10.1039/C9LC00575G.
38 X. Wan, *et al.*, Estrogen Receptor alpha Mediates Doxorubicin Sensitivity in Breast Cancer Cells by Regulating E-Cadherin, *Front. Cell Dev. Biol.*, 2021, **9**, 583572, DOI: 10.3389/fcell.2021.583572.
39 A. Mizielska, *et al.*, Doxorubicin and Cisplatin Modulate miR-21, miR-106, miR-126, miR-155 and miR-199 Levels in MCF7, MDA-MB-231 and SK-BR-3 Cells That Makes Them Potential Elements of the DNA-Damaging Drug Treatment Response Monitoring in Breast Cancer Cells—A Preliminary Study, *Genes*, 2023, **14**, 702, DOI: 10.3390/genes14030702.
40 E. Sobierajska, *et al.*, Unusual Enhancement of Doxorubicin Activity on Co-Delivery with Polyhedral Oligomeric Silsesquioxane (POSS), *Materials*, 2017, **10**, 559, DOI: 10.3390/ma10050559.
41 G. De Renzi, *et al.*, In vitro cultures of circulating tumor cells: a potential tool to unravel drug sensitivity, *Cancer Drug Resist.*, 2022, **5**, 245–260, DOI: 10.20517/cdr.2021.121.
42 M. Yu, *et al.*, Cancer therapy. Ex vivo culture of circulating breast tumor cells for individualized testing of drug susceptibility, *Science*, 2014, **345**, 216–220, DOI: 10.1126/science.1253533.
43 A. Pal, R. Shinde, M. S. Miralles, P. Workman and J. de Bono, Applications of liquid biopsy in the Pharmacological Audit Trail for anticancer drug development, *Nat. Rev. Clin. Oncol.*, 2021, **18**, 454–467, DOI: 10.1038/s41571-021-00489-x.
44 J. Schindelin, *et al.*, Fiji: an open-source platform for biological-image analysis, *Nat. Methods*, 2012, **9**, 676–682, DOI: 10.1038/nmeth.2019.
45 U. Schmidt, M. Weigert, C. Broaddus and G. Myers in *Medical Image Computing and Computer Assisted Intervention – MICCAI*, ed. A. F. Frangi, Springer International Publishing, 2018, pp. 265–273.
46 S. I. R. Lane, *et al.*, Perpetual sedimentation for the continuous delivery of particulate suspensions, *Lab Chip*, 2019, **19**, 3771–3775, DOI: 10.1039/c9lc00774a.

